Two-step deswelling in the Volume Phase Transition of thermoresponsive microgels

Giovanni Del Monte[a,b,c], Domenico Truzzolillo[d,1], Fabrizio Camerin[b,a], Andrea Ninarello[b,a], Edouard Chauveau[d], Letizia Tavagnacco[b,a], Nicoletta Gnan[b,a], Lorenzo Rovigatti[a,b], Simona Sennato[b,a], and Emanuela Zaccarelli[b,a,1]

[a]Department of Physics, Sapienza University of Rome, 00185 Rome, Italy; [b]National Research Council–Institute for Complex Systems (CNR-ISC), Sapienza University of Rome, 00185 Rome, Italy; [c]Center for Life Nano- and Neuro-Science, Fondazione Istituto Italiano di Tecnologia, 00161 Rome, Italy; and [d]Laboratoire Charles Coulomb, UMR 5221, CNRS–Universitè de Montpellier, F-34095 Montpellier, France

Edited by David A. Weitz, Harvard University, Cambridge, MA, and approved August 4, 2021 (received for review May 23, 2021)

Thermoresponsive microgels are one of the most investigated types of soft colloids, thanks to their ability to undergo a Volume Phase Transition (VPT) close to ambient temperature. However, this fundamental phenomenon still lacks a detailed microscopic understanding, particularly regarding the presence and the role of charges in the deswelling process. This is particularly important for the widely used poly(*N*-isopropylacrylamide)–based microgels, where the constituent monomers are neutral but charged groups arise due to the initiator molecules used in the synthesis. Here, we address this point combining experiments with state-of-the-art simulations to show that the microgel collapse does not happen in a homogeneous fashion, but through a two-step mechanism, entirely attributable to electrostatic effects. The signature of this phenomenon is the emergence of a minimum in the ratio between gyration and hydrodynamic radii at the VPT. Thanks to simulations of microgels with different cross-linker concentrations, charge contents, and charge distributions, we provide evidence that peripheral charges arising from the synthesis are responsible for this behavior and we further build a universal master curve able to predict the two-step deswelling. Our results have direct relevance on fundamental soft condensed matter science and on applications where microgels are involved, ranging from materials to biomedical technologies.

soft colloids | polymer networks | volume phase transition | coarse-grained modeling

Responsive particles have recently captured the interest of scientists working under many diverse fields (1–3). Indeed, their ability to adapt to the environmental conditions has enormous advantages for potential applications from biochemistry to nanomedicine (4–7), but also as smart sensors for various analytes (8, 9). The versatility of these soft objects lies in the manifold routes in which the chemical components can be synthesized and in the transfer of the single-particle properties to the mesoscopic and macroscopic level.

In particular, most of these responsive particles are macromolecular colloids, whose inner structure relies on a polymeric system that controls the behavior at the colloidal scale. The prototypical example, that is most actively studied in the literature nowadays, is that of microgel particles, i.e., colloidal-scale realizations of a cross-linked polymer network (10, 11). In their most elementary version, these microgels are composed of a single monomeric component. Among all possible compounds, poly(*N*-isopropylacrylamide) (pNIPAM) is thermoresponsive and undergoes a solubility transition from good to bad solvent conditions at a temperature $T_c \sim 32\,^{\circ}\mathrm{C}$. For responsive microgels, this phenomenon is called volume phase transition (VPT), by which particles are able to reversibly swell and deswell across T_c. Microgels can be routinely synthesized in a wide range of sizes roughly going from 50 nm to 100 μm in diameter, a reason for which they are applicable to a variety of purposes and can be investigated with different experimental techniques, from neutron (12) and X-ray scattering (13) up to optical methods and microfluidics (14). In addition, their complex internal structure and collective behavior, involving particle deformation and interpenetration, can nowadays be resolved with single-particle detail thanks to recent advancements in superresolution microscopy (15–18). The possibility to be studied with these fascinating tools makes them also one of the favorite model systems for fundamental science both in bulk suspensions (11, 19) and adsorbed at interfaces (20–22).

For all the above reasons, it is legitimate to say that the VPT occurring in pNIPAM microgels is one of the most studied phenomena in soft condensed matter. Despite the huge amount of experimental and theoretical work on this topic, which is witnessed by the large number of recent reviews (23–28), there are still fundamental aspects of the VPT that remain poorly understood. In particular, pNIPAM microgels are often treated as neutral systems, since electrostatic interactions are usually thought not to play an important role in their behavior, apart from the stabilization against aggregation given to the suspension, especially at high temperatures. However, the typical batch synthesis procedure of pNIPAM microgels usually includes charged compounds, in particular those from the initiators of the polymerization process. While their presence may be effectively neglected or screened out by the addition of salt (13), recent works pointed out a relevant effect of peripheral charges in concentrated suspensions (29). At

Significance

Microgels, colloidal-scale polymer networks, are the prototype soft colloids. When the constituent polymers are thermoresponsive, they undergo a volume phase transition (VPT) from a swollen to a collapsed state at a characteristic temperature, close to ambient one, of great appeal for several applications. To describe this phenomenon, microgels are usually treated as neutral, but here we show that electrostatics needs to be taken into account. In particular, deswelling occurs via a two-step, rather than a homogeneous, particle collapse, mainly driven by peripheral charges located on the microgel corona, for which we also establish a unifying framework encompassing all studied microgels. Our work thus provides a change of perspective to describe these fascinating systems.

Author contributions: D.T. and E.Z. designed research; G.D.M., D.T., F.C., A.N., E.C., L.T., N.G., L.R., S.S., and E.Z. performed research; G.D.M., D.T., F.C., S.S., and E.Z. analyzed data; and G.D.M., F.C., and E.Z. wrote the paper.

The authors declare no competing interest.

This article is a PNAS Direct Submission.

[1]To whom correspondence may be addressed. Email: emanuela.zaccarelli@cnr.it or domenico.truzzolillo@umontpellier.fr.

This article contains supporting information online at https://www.pnas.org/lookup/suppl/doi:10.1073/pnas.2109560118/-/DCSupplemental.

Published September 10, 2021.

present, the influence of these charges on the VPT has not been clarified yet.

To address these gaps, we recently developed a computational method (30) to assemble disordered networks with desired cross-linker concentration and a core–corona structure that closely reproduces experimental behavior (13, 31). After imposing the correct internal structure, we extended our method to properly include the presence of charged monomers with explicit counterions (32), again validating our results in the presence of explicit solvent and comparing with available experiments (33). For these reasons, we are now in the condition to carefully assess the effect of initiator charges on the deswelling mechanism of pNIPAM microgels across the VPT.

By combining simulations with static and dynamic light scattering experiments, here we show that the presence of these charges strongly affects, from a qualitative point of view, the deswelling transition, inducing an inhomogeneous two-step collapse of the microgels with increasing temperature. This is due to the different solvophobicity of pNIPAM and charged groups, respectively, which manifests in the emergence of a minimum in the ratio between the gyration R_g and hydrodynamic R_H radii at the VPT. First of all, we show that such a minimum is absent for neutral microgels. Second, we analyze in detail the role of the charge distribution throughout the microgel network to assess whether the initiator groups are preferentially located on the surface of the microgels, as previously hypothesized (29), but never effectively proven so far. In order to be able to predict the onset of the two-step deswelling, we further study different combinations of cross-linking ratio, charge content, and charge distribution, establishing clear trends in the occurrence of the minimum in R_g/R_H. Notably, we obtain a master curve for the observed minimum for all simulated microgels when we plot it as a function of the average (effective) charge content per chain on the microgel surface, which turns out to be the simplest indicator of the presence of the two-step collapse.

Our work sheds light on the fundamental electrostatic interactions influencing microgel deswelling, which are crucial to correctly describe their assembly and collective behavior at high temperatures. In addition, it opens up the possibility to a priori design microgels with desired characteristics and tunable onset of two-step deswelling, which could be exploited to enhance or adjust the potential applications of microgels as smart micro-objects.

Results

Experimental Results: Swelling Curves and R_g/R_H. The ratio between gyration and hydrodynamic radii is a relevant quantity in polymer science, widely used as a shape index (34, 35). These two lengths differently characterize the average polymer distribution inside the macromolecular volume. While R_g is the radius obtained from the SD of the mass distribution around the center of mass, R_H is an effective size extracted from the self-diffusion coefficient $\bar{D}$ of the particle. For hard spheres (HSs) moving in an ideal continuous solvent, considering a uniform distribution of the mass within the particle, a value of $R_g/R_H \approx 0.77$ is found (36). For pNIPAM microgels obtained through radical polymerization, this quantity at low T is usually smaller than the HS value (37), since particles consist of a denser core with a density profile gradually fading into the corona. The latter is characterized by the presence of long external chains, the so-called dangling ends, that eventually manifest in an increase of the measured R_H, because of their contribution to the drag, but would not affect significantly the value of R_g (38). At high temperatures, instead, where microgels are completely collapsed, the ratio should tend to the homogeneous HS limit. Since these two lengths carry complementary information, it is instructive to compare their behavior for microgels across the VPT, in particular to capture the occurrence of internal inhomogeneities of the macromolecular structure upon collapse.

We start by showing experimental results for the size variation of microgels in Fig. 1, where both R_g (*A*) and R_H (*B*) are reported as a function of temperature T for the different microgel suspensions investigated in this work. We consider pNIPAM microgels synthesized with a fixed amount of potassium persulfate (KPS) as initiator, which brings into the network a negative charge for each radical unit used in the polymerization reaction. We use a reference sample 1) with a molar fraction of KPS equal

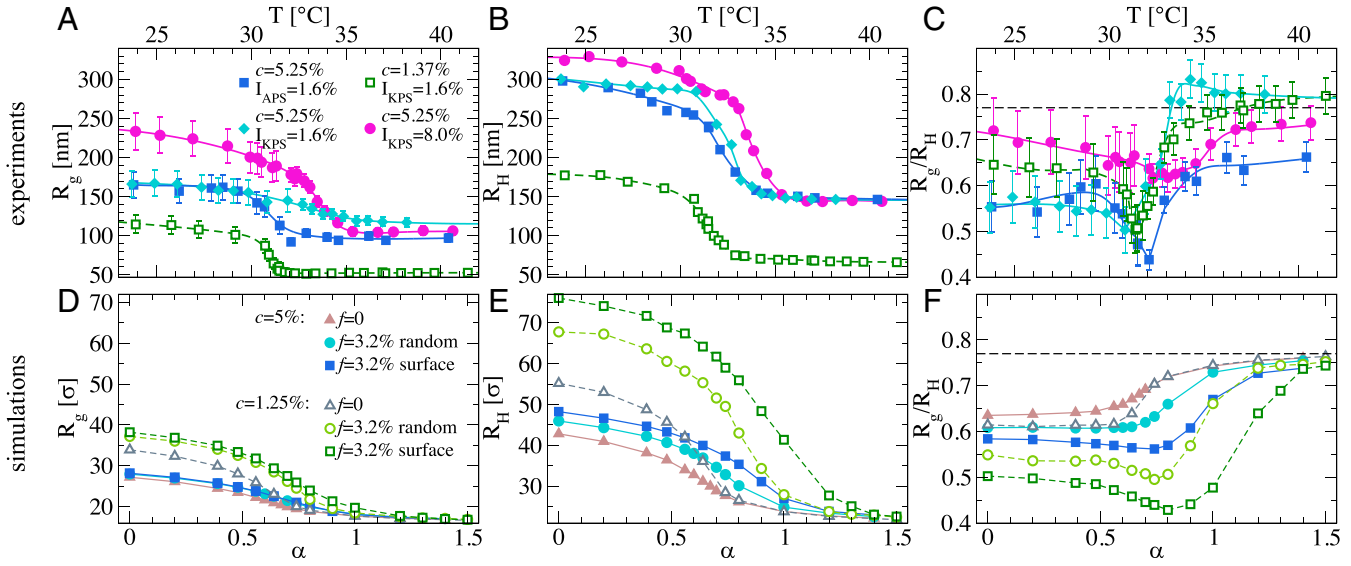

Fig. 1. Swelling curves and R_g/R_H from experiments and simulations. (*A*) Experimental gyration radius R_g, (*B*) hydrodynamic radius R_H, and (*C*) ratio between gyration and hydrodynamic radius R_g/R_H as a function of temperature. Symbols are experimental data, while lines are guides to the eye. Error bars for R_H are smaller than the symbol size; (*D*) numerical R_g, (*E*) R_H, and (*F*) R_g/R_H as a function of the solvophobic parameter α for microgels with $N \sim 42K$ monomers at comparable cross-linker concentrations used in experiments, $c = 1.25\%$ (open symbols) and $c = 5.0\%$ (closed symbols). Lines are guides to the eye. Data refer to neutral microgels ($f = 0$, triangles) and to charged microgels with $f = 0.032$, corresponding to the initiator amount in experiments, but with two different charge distributions: random (circles) and surface (squares). The horizontal dashed lines in *C* and *F* indicate the HS value for R_g/R_H.

to $I_{KPS} = 1.6\%$ and a cross-linker concentration $c = 5.25\%$, in surfactant free conditions. Correspondingly, we vary cross-linker content and initiator content and type, respectively, for three other samples, to systematically assess the effect of each aspect. Namely, we also investigate 2) $I_{KPS} = 1.6\%$ and $c = 1.37\%$ (with added surfactant; *Materials and Methods*), primarily to assess the role of cross-linker; 3) $I_{KPS} = 8.0\%$ and $c = 5.25\%$ to evaluate the role of the amount of initiator; 4) microgels where ammonium persulfate (APS), instead of KPS, is used as initiator, giving the same charge to the polymer network and differing only on the counterion species (NH_3^+ versus K^+). For the latter case, the amount of initiator and cross-linker are the same as in the reference sample ($I_{APS} = 1.6\%$, $c = 5.25\%$).

We observe in Fig. 1*A* that both $c = 5.25\%$ samples with initiator amount of 1.6% have comparable gyration radius of roughly 150 nm. In contrast, the sample with enhanced KPS amount has a much larger gyration radius (~ 250 nm). Concerning the hydrodynamic radius, all three samples with $c = 5.25\%$ have a comparable size, close to 300 nm, and a similar swelling ratio roughly equal to 2, as also shown in *SI Appendix*, Fig. S1. We notice as well that microgels with $c = 1.37\%$ are sensibly smaller, due to the addition of surfactant, and display a larger swelling ratio, as expected for loosely cross-linked microgels. From the swelling curves, we estimate the VPT temperature T_c using a phenomenological function, as described in *SI Appendix*. We find that the VPT temperature associated to R_g depends on the amount of initiator, since $T_c \sim 31\,^\circ$C for $I_{KPS,APS} = 1.6\%$, while it is $\approx 2\,^\circ$C higher for $I_{KPS} = 8\%$. This result can be rationalized by considering the electric charge brought by initiator molecules. Indeed, in agreement with previous studies on charged microgels (33, 39), a shift of T_c to higher values is found when the amount of charges increases. In addition, we observe that, for all studied samples, the VPT transition is encountered at a lower temperature, by $\approx 1.0\,^\circ$C, for R_g with respect to R_H. This could be tentatively interpreted in terms of the presence of charged molecules preferentially on the surface of the network (40), an aspect that will be further analyzed later.

Fig. 1*C* shows R_g/R_H as a function of T for all samples. At low temperatures, all studied microgels display a lower ratio with respect to the HS limit, indicating a less homogeneous mass distribution. We observe a higher value of R_g/R_H both for loosely cross-linked microgels ($c = 1.37\%$) and for those carrying a high amount of charges ($I_{KPS} = 8\%$). The fact that in the former case the particles have a more compact shape, as suggested by the value of R_g/R_H at low T, may be caused by the presence of surfactants. Instead, for the latter case, the larger number of chain ends (constituted by the initiator molecules) may result in shorter chains, which, combined with the small cross-linking effect of KPS (41), may lead to higher monomers density in the corona. However, for large T, all microgels become more and more compact with R_g/R_H tending to converge toward the homogeneous HS value. Although experimental uncertainties prevent us from drawing definite conclusions on the specific values and trends observed for the different samples, we clearly identify that all samples display a minimum in R_g/R_H close to the VPT temperature estimated from the hydrodynamic radius (*SI Appendix*, Table S1). In particular, the three microgels with the same initiator amount display a minimum close to $T_c \sim 32\,^\circ$C, which is instead found at a slightly larger temperature for microgels with $I_{KPS} = 8\%$. Interestingly, in this case, the minimum is rather shallow, as opposed to those of the other samples where it is more pronounced. The presence of a minimum in R_g/R_H has been previously observed in a few experimental studies (42, 43), including one from some of the present authors (44) for large and loosely cross-linked microgels. However, most of such previous studies reported only a few data points around the VPT, so that the presence of the minimum was hinted, but not totally evident. In the present work, the fine resolution in temperature allows us to unambiguously observe the minimum for all samples. This can be interpreted in terms of a nonuniform collapse of the microgels, which could be intuitively attributed to the underlying inhomogeneous core–corona structure of the microgels. An alternative explanation could be found in the role played by the initiator charged groups on the deswelling behavior (29, 44). In particular, arguments in favor of a specific distribution of these charges have been put forward (40, 45, 46), suggesting that during polymerization the charged groups try to minimize their mutual electrostatic repulsion by remaining far from each other, thus being located mostly at the periphery rather than in the core of the microgels. Nonetheless, no direct evidence for the location and the arrangement of these groups has been provided so far.

Numerical Results: Unveiling the Role of Charges. To provide a microscopic understanding of this issue, we rely on numerical simulations. We focus on microgels that closely match the experimental ones, by imposing very similar cross-linking contents, namely $c = 1.25\%$ and 5%. We compare the case of perfectly neutral microgels with charged ones, having the same charged monomers fraction ($f = 3.2\%$) as the initiator groups in experimental systems. For this specific value of f, we also vary the charge distribution by considering a random arrangement of the charges either throughout the network, hereafter named "random charge distribution," or only onto surface chains (*Materials and Methods*), that we refer to as "surface charge distribution." In this way, we are able to assess how the deswelling behavior is affected by the charge arrangement upon increasing temperature.

Our coarse-grained modeling accounts for the presence of a disordered network with a realistic core–corona distribution (13). In the presence of charges, our treatment explicitly includes the presence of counterions, as these turn out to be crucial to provide a proper description of the local inhomogeneities arising in the network (32). In addition, charged monomers do not change their affinity to the solvent as we vary the temperature in order to properly capture the experimental picture (33). A detailed description of the model is provided in *Materials and Methods*.

Numerical results for the radius of gyration R_g are reported in Fig. 1*D* as a function of the solvophobic parameter α, which plays the role of an effective temperature in simulations. As expected, the gyration radius is found to be mostly influenced by the cross-linker concentration, with R_g being much larger for $c = 1.25\%$ than for $c = 5\%$. On the other hand, the presence of charges has a small effect on the gyration radius, which increases only slightly with f. Notably, the effect of charge arrangement within the network is almost absent, being R_g very similar for random and surface distributions. To estimate numerically R_H, we rely on an operative definition that is discussed in *Materials and Methods* and further validated in *SI Appendix* also by comparing to previously published data (13) (*SI Appendix*, Figs. S3 and S4). The resulting R_H are reported in Fig. 1*E* as a function of the solvophobic parameter α, displaying a behavior that looks rather similar to that of R_g. An important difference, however, arises when comparing the two different charge distributions. Indeed, we find a significant increase of R_H in the presence of a surface charge distribution compared to the case with random charges due to the accumulation of charges in the corona of the microgel, which keeps the latter much more expanded.

The calculated ratio R_g/R_H is shown in Fig. 1*F* as a function of α. First of all, we notice that our numerical definition of R_H allows us to obtain estimates for the ratio R_g/R_H that are, within statistical uncertainties, in reasonable agreement with experimental ones and that correctly tend to the HS value at

large α in all cases. While we observe the emergence of a minimum in under specific conditions of charge content f and charge distribution, it is important to highlight that such a minimum is completely absent for perfectly neutral microgels, independently of the value of c. This result allows us to unambiguously exclude that the appearance of the minimum stems from the underlying core–corona topology of the microgels. Rather, it turns out to be related to the presence of the initiator charges, which therefore plays an explicit role in the VPT of pNIPAM microgels. Such a role, not often recognized in the literature, appears to be important to properly capture the internal modifications of the microgels upon collapse, as also confirmed by electrophoretic mobility measurements across the VPT for a subset of the samples investigated in this work (*SI Appendix*, Fig. S2) (44, 47).

By examining in more detail the specific features of the microgel for which a minimum in R_g/R_H is present, we find that, for both studied values of c, microgels with charges arranged on the surface display a very pronounced minimum that occurs roughly at the VPT in agreement with experimental findings. Instead, for randomly located charges, the presence of a minimum is evident only for $c = 1.25\%$, while it is absent for $c = 5.0\%$. Since a minimum is observed for all samples in experiments, this suggests that initiator charges are not randomly spread throughout the network, but rather they are preferentially located close to the microgel surface.

Microscopic Origin of the Two-Step Collapse. In order to unveil the microscopic mechanism that gives rise to the presence of a minimum in R_g/R_H, we analyze the microgels by selecting different regions within their volume and calculating their relative swelling in a so-called "local swelling" approach. We define the internal regions by fixing the number of particles within each of them on the basis of their distance from the center of mass, so that, upon varying α, we monitor the true volume variation of a given portion of the microgel. The three regions are defined as follows: (region I) the "core" region roughly having the same volume as a sphere of radius equal to the gyration radius; (region II) the "inner corona" region, corresponding to an intermediate shell, whose volume—together with that of the core—roughly coincides with that delimited by the hydrodynamic radius; and (region III) the "outer corona" shell. More details on the choices of the three regions are given in *Materials and Methods* and in *SI Appendix* (*SI Appendix*, Fig. S5).

We start by discussing the behavior of neutral microgels. For both values of the examined cross-linked concentrations, reported in Fig. 2 *A* and *D*, we observe that the deswelling transition, monitored by the volume change of each region, occurs roughly at the same value of the solvophobic parameter for all regions. These results indicate that a purely neutral microgel deswells in a homogeneous fashion, independently on the internal structure and thus on its intrinsic core–corona topology. This is due to the fact that all monomers experience the same affinity to the solvent, which induces a simultaneous collapse of the whole particle. No difference is observed between the two values of c, except for a more pronounced swelling ratio for the less cross-linked microgels, as expected.

We now turn to the surface-charged microgel with $f = 3.2\%$, whose local swelling behavior is reported in Fig. 2 *B* and *E*. In this case, it is evident that the collapse of the three regions does not occur simultaneously, with the core (region I) showing a deswelling transition that takes place at a sensibly lower value of α with respect to the outer corona (region III). In addition, a clear difference is present for the two values of c regarding the inner corona region (region II): While its collapse is approximately the same as that of the core for $c = 5\%$ (panel *E*), a clear delay in α is present for the less cross-linked microgel (panel *B*). In the latter case, a clear sequence of inflection points is found when going from the inner to the outer region. Similarly to the neutral case, we still observe that the behavior of the sphere of radius R_g roughly follows that of the core, while that of radius R_H is very close to that of the corona region. These results clearly show that the development of a minimum in the ratio between R_g and R_H, as reported in Fig. 1, can be easily interpreted in terms of the different collapse behavior that involves, respectively, the core and the corona region, the latter intended as a whole.

We thus refer to this phenomenology for simplicity as a "two-step" collapse, although the number of steps may depend on

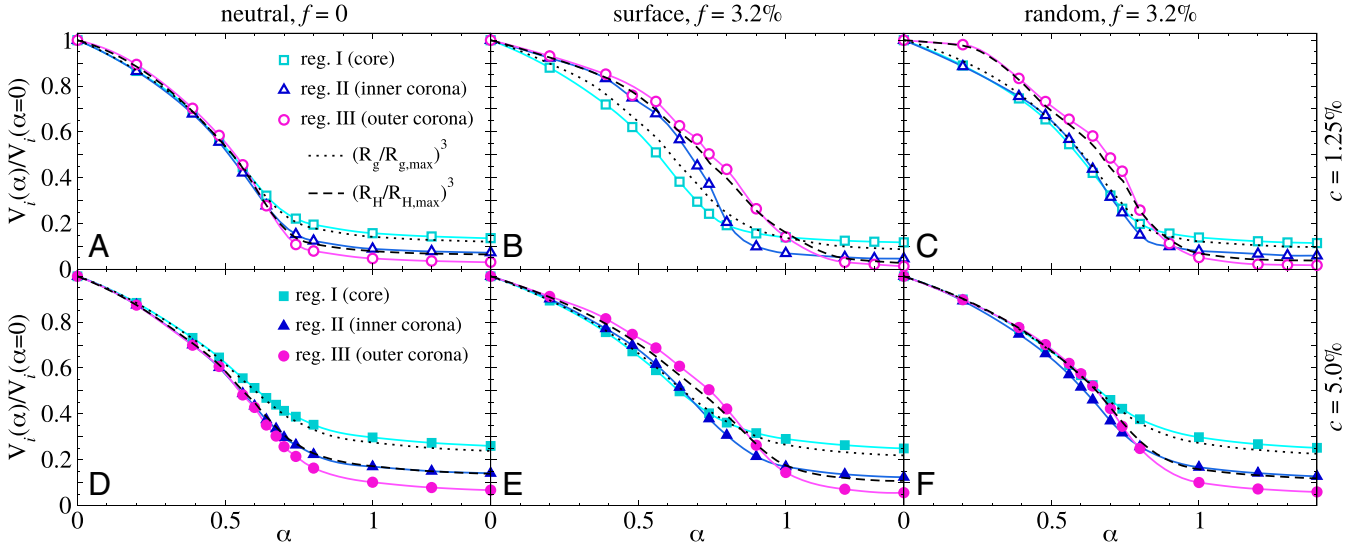

Fig. 2. Local swelling curves. Normalized volume for the three different regions, defined as $V_i(\alpha)/V_i(0)$ where V_i refers to the volume of the ith region, labeled as i = I, II, III for core, inner, and outer corona regions, respectively. Top row panels refer to microgels with $c = 1.25\%$ and different charge distributions: (*A*) neutral ($f = 0$), (*B*) surface ($f = 3.2\%$), and (*C*) random ($f = 3.2\%$). Bottom row panels are for microgels with $c = 5.0\%$ and different charge distributions: (*D*) neutral ($f = 0$), (*E*) surface ($f = 3.2\%$), and (*F*) random ($f = 3.2\%$). The black lines correspond to the volume ratios of spherical regions corresponding to the gyration radius (dotted lines) and to the hydrodynamic radius (dashed lines).

the level of heterogeneity of the underlying microgels. Its microscopic origin can be traced back to the different affinity of the charged monomers with respect to the solvent and to their different electrostatic screening conditions. Indeed, since charges remain solvophilic at all values of α and are accumulated in the corona, this provides the microgel with a heterogeneous collapse mechanism that differentiates the core (where charges are absent) from the corona (where most of the charges are located).

While surface-charged microgels unambiguously show a two-step collapse for both studied c values, the situation is different for randomly charged microgels with $f = 3.2\%$, reported in Fig. 2 *C* and *F*, which display a different behavior according to the value of c. Indeed, for $c = 1.25\%$ the outer corona is found to undergo a deswelling transition at a larger value of α with respect to the core, while this is not the case for $c = 5\%$. This is reflected in the occurrence of a minimum in R_g/R_H only for the randomly charged case with $c = 1.25\%$, with this being absent for $c = 5\%$, as previously shown in Fig. 1*F*.

To further confirm that the presence of the minimum is associated to a nonhomogeneous internal deswelling of the microgels, we report the snapshots of randomly charged microgels for the two studied c values in Fig. 3. Starting with the $c = 1.25\%$ microgel, we clearly see that long dangling chains remain in rather extended configurations even when the internal portions of the networks have already collapsed. This is also evident at α values slightly above the VPT, where both core and inner corona are found in a compact spherical shape, while the outer chains are still protruding out of the sphere, giving the microgel an anisotropic global structure. It is instructive to focus on the outer corona monomers at intermediate values of α, where the external chains are formed by a mixture of collapsed and extended regions, due to the different solvophobic interactions of charged and neutral monomers, respectively. Although the charge distribution is random, the large amount of long chains in a low–cross-linked microgel (*SI Appendix*, Fig. S6) makes it favorable to have several charged groups in these regions. This triggers the onset of a minimum in R_g/R_H, precisely by the same mechanism occurring in surface-charged microgels. However, such behavior is not observed for $c = 5\%$, where the larger amount of cross-linkers limits the chain length in the corona region, thus inhibiting the mutual influence of charges on the dangling chains, as also visible in the snapshots of Fig. 3, illustrating a rather homogenous deswelling for the $c = 5\%$ randomly charged microgel at all values of α. For comparison, corresponding snapshots for surface-charged microgels are reported in *SI Appendix*, Fig. S7.

On the basis of the above evidence, we can thus associate the occurrence of a minimum in R_g/R_H to the two-step collapse of the microgel, differentiating core and corona behavior. While the underlying topology is not responsible for such a mechanism, it facilitates its onset even for randomly charged microgels at low c, due to the more heterogeneous nature of the network under these conditions.

Effect of Cross-Linker Concentration, Charge Amount, and Charge Distribution on the Minimum in R_g/R_H. In the previous subsection, we provided evidence that the presence of charged groups is a necessary condition for the occurrence of a minimum in R_g/R_H, but also that this depends on the specific charge distribution and on the cross-linker concentration. While for microgels decorated with surface charges for $f = 3.2\%$, we observed the minimum for both studied values of c, which can be intuitively understood in terms of the delayed collapse of charged surface chains, the situation is more complex for randomly charged microgels, where the presence of the minimum is found to depend also on c. To shed light on this aspect, we perform additional simulations of microgels with random charge distributions and investigate the effect of varying f as well as c. The behavior of R_g/R_H as a function of effective temperature α is reported in Fig. 4 *A*–*C* for a large variety of microgels, with c varying between 1.25% and 10% and f exploring a range from 1% to 10%.

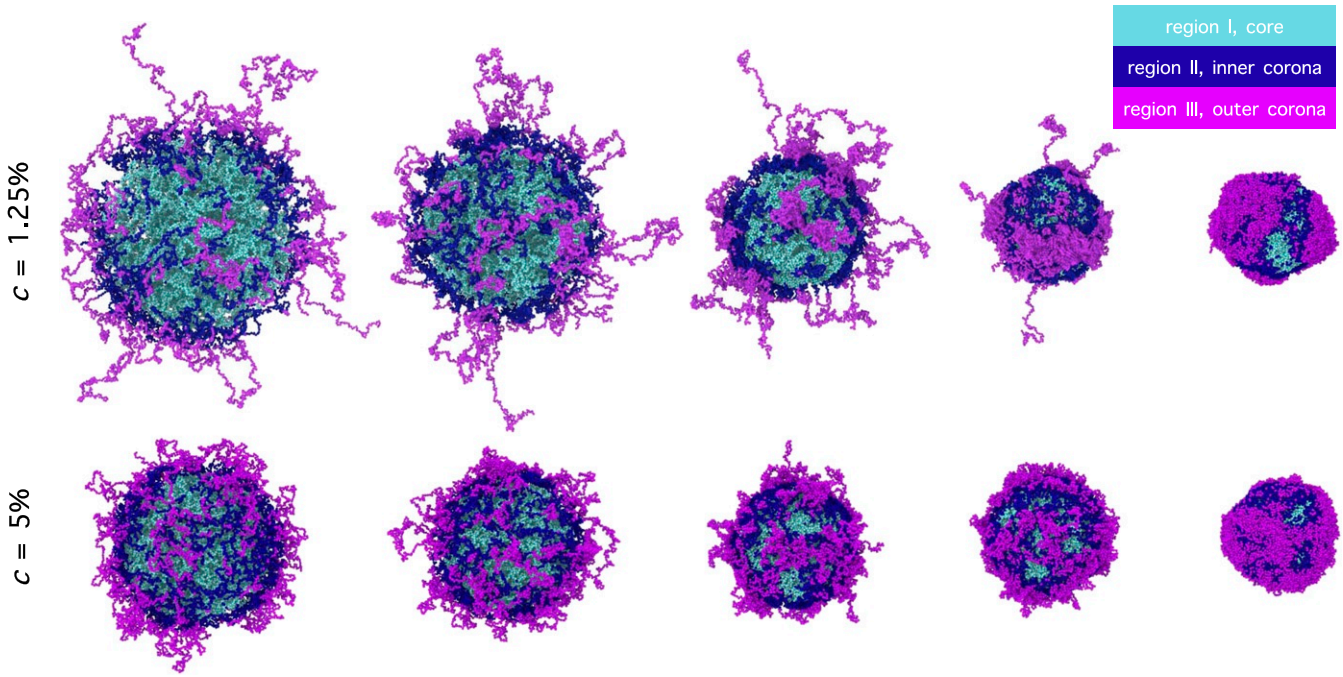

Fig. 3. Snapshots of randomly charged microgels across the VPT illustrating the local swelling for $f = 3.2\%$ and two values of c for different α from the swollen to the collapsed state. From *Left* to *Right*, for $c = 1.25\%$, $\alpha = 0, 0.48, 0.74, 0.90, 1.20$, while for $c = 5\%$, $\alpha = 0, 0.48, 0.74, 0.80, 1.20$. Monomers are colored according to the region they belong to: cyan indicates the core region; blue the inner corona region; purple the outer corona region. All snapshots refer to equilibrium states.

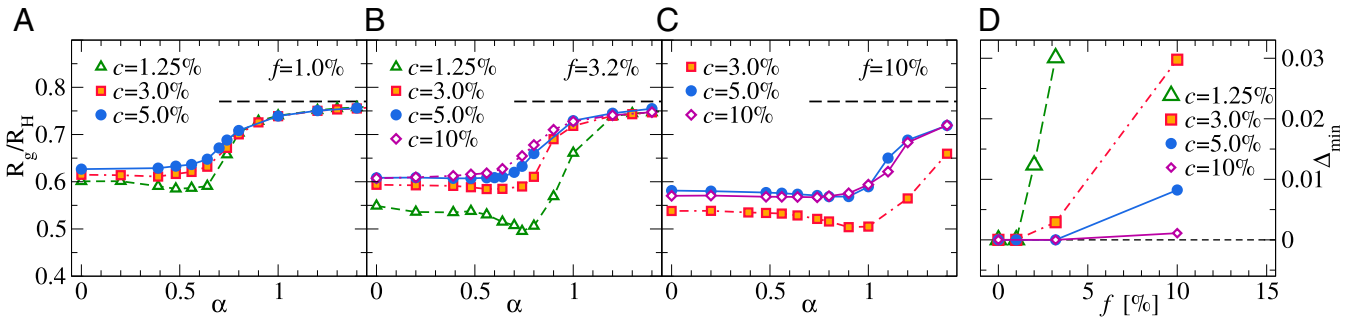

Fig. 4. Ratio R_g/R_H for randomly charged microgels as a function of the solvophobic parameter α for (*A*) $f = 1.0\%$, (*B*) $f = 3.2\%$, and (*C*) $f = 10\%$ and different values of c. The dashed lines indicate the HS value. (*D*) Depth $\Delta_{\min}$ of the minimum in R_g/R_H as a function of f for different c. The corresponding swelling curves are reported in *SI Appendix*, Fig. S8.

We observe that, upon decreasing c while leaving f unchanged, the minimum becomes more and more evident, in agreement with unpublished experimental results (43). In addition, Fig. 4 shows that the minimum is more pronounced with increasing f at the same value of c, also shifting to larger and larger values of α. In all cases, the decrease of R_g/R_H at the minimum is also accompanied by its decrease at small α, indicating that the growth of R_H is not compensated by that of R_g under swollen conditions. At large α, most curves tend to recover the HS value, except for the most charged microgels, which are expected to completely collapse at much larger effective temperatures (33, 39), beyond those explored in the present simulations.

From all data in Fig. 4, we can build a plot reporting the depth of the minimum $\Delta_{\min}$ (defined in *Materials and Methods*) as a function of charge content, reported in Fig. 4*D*, for different values of c, identifying regions in the (c, f) parameter space where no minimum is observed (homogeneous deswelling), as opposed to others where this is present (two-step deswelling). Clearly, no minimum is found for low c and low f. However, at very large c, the minimum is also inhibited for very large charge content. Finally, the results in Fig. 4 allow us to exclude the presence of a minimum in R_g/R_H for highly cross-linked charged microgels.

Having shown that the minimum arises also in randomly charged microgels above a certain charge fraction for each considered c, we now further clarify the role of the specific charge distribution by tuning it ad hoc. To this aim, we investigate $c = 5\%$ microgels where charges are located on the surface but with the additional constraint that a fixed number of charges per (surface) chain should be present, varying this number from 1 to 3. In this way, we want to assess the role played by charge correlations and whether there exists a minimum amount of charges per chain required to observe the minimum in R_g/R_H. The behavior of R_g/R_H for these cases is reported in Fig. 5*A*, where we clearly find confirmation that there is no minimum when only one charge per chain is present, even if they are all located on the surface (as shown by the charged monomers radial distributions in *SI Appendix*, Fig. S9). A tiny minimum appears when two charges per surface chain are present and finally a well-defined minimum occurs for three charges per chain. The systematic increase of the number of charges per surface chain makes the behavior of R_g/R_H more and more similar to the originally considered case of surface charges that are randomly distributed throughout the corona, thus mimicking the experimental situation of a pNIPAM microgel with a given amount of initiator arranged on the outer part of the microgel surface in a disordered fashion. Not only the minimum becomes more pronounced, but its position also moves toward larger effective temperatures. Additional data for $f = 10\%$ and "mixed" charge distribution (partially located on the surface and partially random) are reported in *SI Appendix* (*SI Appendix*, Fig. S10).

It is important to notice that, in the case of standard surface charge distribution with $f = 3.2\%$, the average charge per surface chain is roughly equal to $\sim -1.4e^*$ only. However, the minimum is much more pronounced in this case than when the charge is set to be $-3e^*$. In this case, the variance of the number of charges per chain is not negligible, as displayed in Fig. 5*B*. In this plot, we report the distribution of the number of charges per chain for random and surface charge distributions with varying c and f, showing that all curves referring to microgels not displaying the two-step collapse are rather well described by a single exponential decay, while those with a well-developed minimum reveal the onset of a tail in the distribution. This suggests the development of a characteristic correlation between charges on long chains, which makes the heterogeneous deswelling mechanism much more efficient. The SD of the distribution of charges per chain is further enhanced at $c = 1.25\%$, due to the underlying network topology, making the minimum in R_g/R_H always more pronounced for low–cross-linked microgels than for the corresponding ones at higher c.

To visualize what happens at the level of single chains, we show in Fig. 6 the snapshots of microgel cross-sections for different values of α. In particular, we compare random and surface charge distributions with $f = 3.2\%$ and $c = 5.0\%$, and we draw with the same color charges belonging to the same chain. In this way, we aim to visualize the presence of multiple charges per chain and how the deswelling process is affected. We see that for randomly charged microgels the charged chains, despite

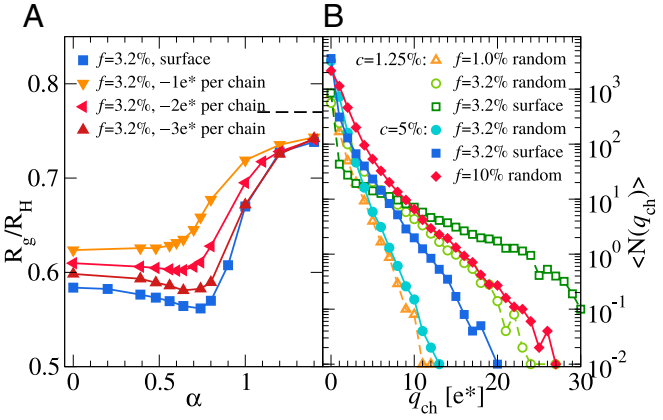

Fig. 5. Ratio R_g/R_H for c = 5% surface-charged microgels (*A*) and distribution $N(q_{ch})$ of number of charges per chain. The dashed line indicates the HS value. (*B*) Surface-charged microgels are shown with filled symbols, while open triangles indicate microgels with $f = 3.2\%$ for which charges are constrained to be found as one, two, or three charges on each external chain, indicated as $-1e^*$, $-2e^*$, $-3e^*$ per chain, respectively.

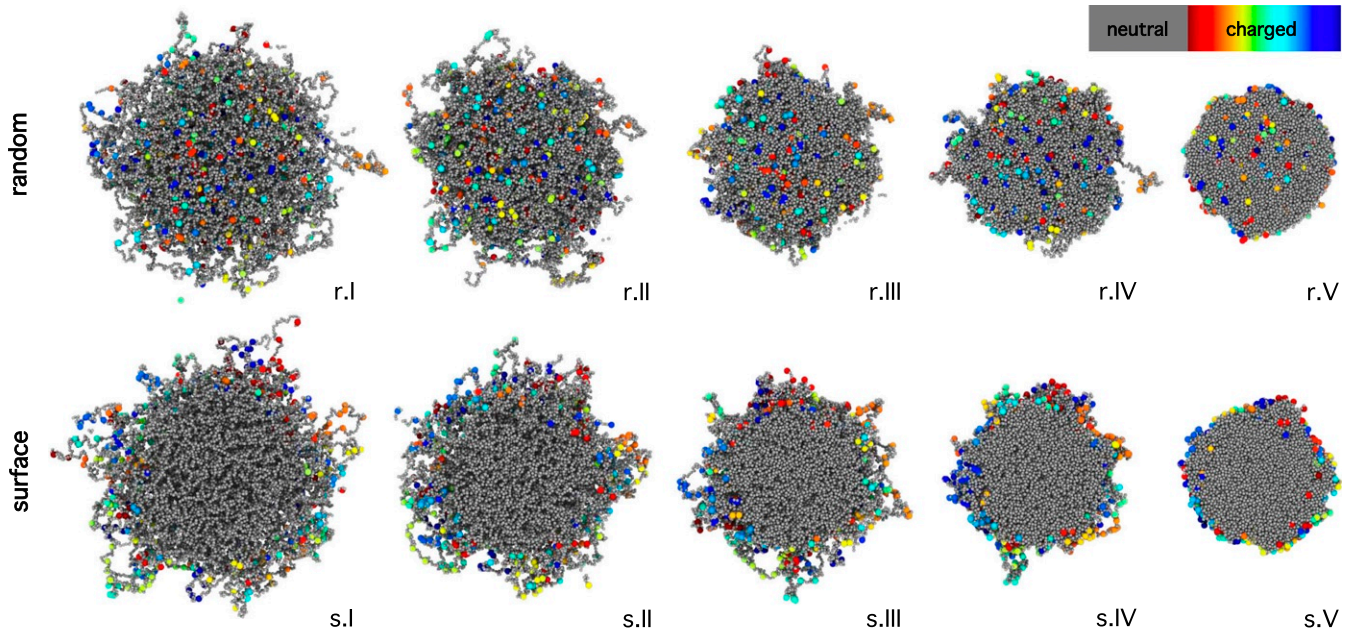

Fig. 6. Snapshots highlighting charged beads. Simulation snapshots representing cross-sections of microgels with $f = 3.2\%$ and $c = 5\%$ with random (top row) and surface (bottom row) charge distribution referring to different values of the swelling parameter $\alpha = 0$, 0.48, 0.74, 0.80, 1.20 from the swollen to the collapsed state (from *Left* to *Right*). Charges belonging to the same chain are shown with the same color and enhanced size, to improve their visualization, while uncharged monomers are gray.

a few isolated cases, play a minor role in the overall collapse of the network, probably because they are rare and pulled by the neighboring neutral monomers toward the collapsed network with increasing α. Instead, for surface charged microgels, there are many more charged chains, each in turn with several charged monomers that prevent the chains from a full collapse. These microgels are thus found to maintain an extended conformation up to large values of α, even beyond the VPT. Hence, prior to the final collapse at very large α, the microgel clearly looks like an inner compact sphere with many elongated chains (see, for instance, Fig. 6, s.IV).

Predicting the Two-Step Collapse: A Simple Indicator. To take full advantage of the predictive ability of the simulations, we are now in the position to establish an indicator that may be useful in predicting the appearance of the minimum in R_g/R_H. Since we demonstrated that the two-step collapse is due to the explicit presence of charged groups in the microgels and preferentially to their arrangement on the microgel corona, we propose to identify the average number of charges per chain on the microgel surface, defined as $\langle q_{\rm ch}\rangle_{\rm out}$ as the observable that controls the onset and the development of the minimum. To verify that this is the case, we plot the dependence of the minimum depth $\Delta_{\rm min}$ as a function of $\langle q_{\rm ch}\rangle_{\rm out}$ in the *Inset* of Fig. 7. We find that microgels with the same charge distribution, either surface or random, independently of their values of c and f, display characteristic behaviors that are roughly monotonic in $\langle q_{\rm ch}\rangle_{\rm out}$, except when this is very large in the case of randomly charged microgels (see below). We also notice that no minimum is observed when $\langle q_{\rm ch}\rangle_{\rm out} \lesssim 1$, meaning that on average more than one charge per surface chain is needed in order to develop the onset of the two-step collapse. Then, as $\langle q_{\rm ch}\rangle_{\rm out}$ increases, the depth of the minimum gets more and more pronounced both for surface-charged microgels and for those where we impose a fixed number of charges per chain. A similar behavior is observed for microgels with random charges at low f content, and thus low $\langle q_{\rm ch}\rangle_{\rm out}$. However, when this increases, we find first a sudden growth of $\Delta_{\rm min}$, which even exceeds that of surface-charged microgels at the same $\langle q_{\rm ch}\rangle_{\rm out}$, followed by a drastic reduction and a highly nonmonotonic behavior, calling for a further refining of the chosen indicator.

To this aim, we exploit the explicit charge treatment in our simulations and consider the screening effect of the counterions, so that rather than the bare charge, we consider an effective charge per surface chain $\langle q_{\rm ch}^{\rm eff}\rangle_{\rm out}$ (*Materials and Methods* and *SI Appendix*). Therefore, in Fig. 7, we plot the minimum depth $\Delta_{\rm min}$ as a function of $\langle q_{\rm ch}^{\rm eff}\rangle_{\rm out}$. Remarkably, a master plot is found where data for all simulated microgels (24 different systems in total) fall on the same curve manifesting the same behavior. We notice that a couple of points are found to slightly deviate from the master curve, which may well be attributed to the statistical uncertainty of our calculations, which are carried out for a single topology and charge realization for each microgel. However, it is noteworthy that the use of the effective charge is

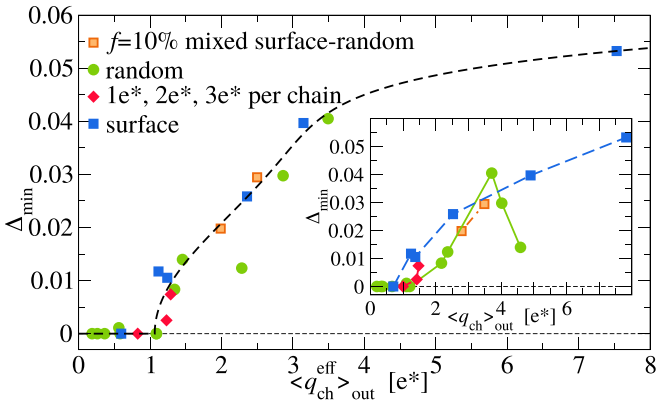

Fig. 7. Prediction of two-step collapse. Master plot for the minimum $\Delta_{\rm min}$ as a function of the average effective charge $\langle q_{\rm ch}^{\rm eff}\rangle_{\rm out}$ of the surface chains. Lines are guides to the eye. (*Inset*) Same as in the main panel but for the bare charge $\langle q_{\rm ch}\rangle_{\rm out}$.

able to completely remove the nonmonotonicity of the data for randomly charged microgels as a function of bare charge, indicating the overall correctness of our procedure. In this respect, we remark that this is due to the fact that screening effects are much more effective for random rather than for surface charged microgels, which can be intuitively understood in terms of an overall reduced electrostatic repulsion experienced by the counterions when charges are distributed throughout the entire network, thus facilitating the microgel collapse.

Discussion

In this work, we thoroughly investigated the swelling behavior of microgels across the VPT upon varying cross-linker concentration and charge distribution. The study was motivated by experimental measurements of gyration and hydrodynamic radii that showed the appearance of a characteristic minimum in the ratio R_g/R_H at a temperature close to the VPT one. Such a minimum indicates that a different rate of collapse with increasing temperature takes place between the inner mass of the microgel, quantified in size by the gyration radius, and its outer mass, associated to the hydrodynamic radius. Similar evidence was also reported in few previous works (42, 43), but its microscopic origin was not investigated in detail so far. The new experimental measurements reported in this paper for four different samples unambiguously reveal the presence of such a minimum. In a previous work by some of us (44), the minimum was tentatively associated to the presence of initiator charges, manifesting their effect under collapsed conditions even for simple pNIPAM microgels. This conjecture was supported by electrophoretic mobility measurements also displaying a rapid increase of the signal for temperatures above the VPT, thus providing evidence that, in the high temperature regime, pNIPAM microgels have to be considered as charged micro-objects (29, 47, 48). However, a legitimate doubt concerned whether the minimum in R_g/R_H would be solely due to charges or could be attributed to other ingredients, such as the inhomogeneous core–corona topology of pNIPAM microgels synthesized by precipitation polymerization methods. For these reasons, the primary purpose of the present work was to correctly assess the role of charges on the occurrence of the minimum.

We thus performed an extensive set of simulations for several realistic microgels, with different cross-linker concentration, charge content, and distribution. First of all, we found that the minimum does not occur for purely neutral microgels, even for very low–cross-linked concentrations (like $c = 1.25\%$, the lowest value investigated in this work), where the inhomogeneous internal structure of the microgels is enhanced. Hence, we can safely exclude that the two-step collapse is associated to the topology, whereas it must be attributed to additional interactions emerging at the VPT, which modify the homogeneous deswelling that would take place in a perfectly neutral microgel. Incidentally, it is important to notice that, to our knowledge, it is currently not possible to synthesize strictly uncharged microgels made of pNIPAM, the only example being for microgels made of (nonthermoresponsive) polystyrene (49), thus preventing confirmation of the present numerical predictions for neutral microgels. Alternatively, experiments could be performed in the presence of added salt that would screen electrostatic interactions (48), although at the same time favoring microgel–microgel aggregation at high temperatures.

The additional mechanism giving rise to the two-step deswelling is thus attributed to electrostatic effects. In particular, charged initiator groups interact with the solvent in a different way than NIPAM monomers as temperature increases, since they always maintain a solvophilic character, thus acting against collapse. When the amount of initiator is very low, as in common synthesis procedures, these effects can be very subtle and may depend on the location of these charges. Therefore, it is important to discriminate between random location of charges throughout the network and surface arrangement at the periphery of the corona. Indeed, the latter case seems to be appropriate to model charged initiators, which start the polymerization process and then possibly remain confined in the outer part of the microgel to minimize mutual electrostatic interactions. In this way, being localized on the surface, upon particle collapse the charged groups would experience a strong mutual repulsion, thus influencing the corona deswelling as demonstrated in the previous sections. On the other hand, a random distribution of charges would "dilute" the effect of the electrostatic contribution throughout the whole particle, including the core, unlikely affecting the collapse of the particle during the VPT.

The simulation results presented here clearly show that, for typical amounts of initiators used in synthesis of pNIPAM microgels ($f = 3.2\%$) and standard cross-linker concentration (c = 5%), a random distribution of charges does not give rise to a minimum in R_g/R_H, while this is present when charges are distributed only on the surface. Actually, the minimum for random charge arrangement only manifests at much higher f or lower c, a numerical prediction that awaits experimental confirmation. In this respect, it would be useful to perform measurements of R_g/R_H for ionic microgels, e.g., in the presence of a second component such as PAAc. In this case, due to different reaction rates, the comonomers might still be inhomogeneously distributed (50), so it remains to be verified whether a random distribution of charges may still describe certain cases.

On the other hand, our simulations showed that microgels with surface charge distribution seem to be the appropriate model to describe the occurrence of the minimum in R_g/R_H for pNIPAM microgels, in agreement with experimental measurements and with previous hypothesis (40, 46, 51), although a direct proof of charge location in experiments would be very valuable. To this purpose, superresolution microscopy experiments (15) could be helpful when combined with selective labeling of the surface or even of the initiators, as well as studies where the average bare charge and screening electrostatic conditions of the polymer chains would be systematically varied, as recently done in ref. 52. Additionally, one could rely on neutron scattering measurements, where differentiations of the molecular components could be achieved by contrast variation (38, 53, 54). The numerical results of the present work will further provide a framework to interpret experimental data thanks to the master curve reported in Fig. 7, which makes use of a single quantity, the screened average charge per surface chain $\langle q_{\mathrm{ch}}^{\mathrm{eff}} \rangle_{\mathrm{out}}$, to describe the two-step deswelling process. These experiments could also be used to estimate such an effective charge.

Another important point to be addressed in the future concerns the systematic variation of the amount of initiator, a relatively unexplored parameter. It will be interesting to see to which extent it can be exploited, given that too large amount of initiator could give rise to synthesis by-products that would not necessarily be part of the microgel network. In addition, it could be possible that above some threshold, the charges would start to penetrate in the interior of the microgel giving rise to "mixed" surface-random distribution, as discussed for instance in ref. 45. Indeed, looking at the experimental behavior for $I_{\mathrm{KPS}} = 8\%$ (Fig. 1), we observe that this sample displays larger values of R_g/R_H at low temperatures and a shallower minimum at the VPT, in qualitative agreement with the effect of mixed charge distributions shown in *SI Appendix*. These findings seem to suggest that increasing the initiator molar fraction in the synthesis does not simply give rise to an augmented charge distribution peaked at the microgel periphery, but presumably homogenizes the initiator (and possibly the mass) distribution radially within the microgel.

Finally, the outcomes of this work will also be relevant for the study of the collective behavior of pNIPAM microgels at high temperatures, where numerical/theoretical works are currently lacking. While it is now established that the effective potential for swollen microgels can be described as a soft repulsion (19, 55), at high temperatures attractive interactions should become important (51, 56), albeit mediated by the electrostatic interactions of the initiator. It will be therefore necessary to appropriately assess their contribution to the collective and rheological behavior of dense microgel suspensions.

Materials and Methods

Synthesis. Surfactant-free radical polymerization has been used to synthesize different batches of pNIPAM microgels. Specifically, we used methylene-bis-acrylamide (BIS) as cross-linker agent and two cationic initiators: potassium persulfate ($K_2S_2O_8$) (KPS) and ammonium persulfate [$(NH_4)_2S_2O_8$] (APS). Three different batches with $c = 5.25$ mol% of BIS have been synthesized with the following initiator content and type: 1.6 mol% of KPS; 1.6 mol% of APS; 8.0 mol% of KPS. Since our main focus is to scrutinize the role of initiator charges, we primarily use microgels obtained via surfactant-free emulsion polymerization, which allows us to minimize the impact of residual ionic surfactants on microgel deswelling. However, we also carried out one synthesis in the presence of surfactant and used the sample after purification, in order to test the possible impact of surfactant addition, while at the same time reducing both the microgel size for low cross-linker content and the associated error on the R_g measurement. In this way, we obtained a batch of smaller particles, which has been prepared through the addition of an amount of 0.85 mol% of sodium dodecyl sulfate (SDS). In this case, microgels are synthesized with $c = 1.37$ mol% of BIS and 1.6 mol% of KPS. All samples have been further purified through three consecutive cycles of centrifugation and supernatant replacement with deionized water. Finally, 2 mmol of sodium azide NaN_3 have been added to the final samples to prevent bacterial growth.

Experiments. To characterize the structure of particles in suspension, we employed static light scattering (SLS) and dynamic light scattering (DLS). For all the samples, an aliquot of the mother batches (1 wt% of NIPAM) has been diluted 60 times so to reach a mass fraction of 0.017 wt% of NIPAM, equivalent to microgel volume fractions lower than 0.4% as determined by viscosimetry following the method detailed in ref. 57. All scattering experiments have been performed by using the same laser source ($\lambda = 532$ nm). Before each data acquisition, each sample has been thermostatted for 20 min via a recirculating bath with 0.1 °C accuracy and light has been collected by varying the scattering angle for SLS measurements with 1 ° accuracy. We extracted the average gyration radius of microgels, fitting the low scattering-vector part of the intensity $I(q)$ with the functional form (Guinier approximation) as discussed in *SI Appendix* (*SI Appendix*, Fig. S11). For all samples, data could be reliably fitted in the entire range $5.5\ \mu m^{-1} \leq q \leq 2/R_g$. The uncertainty on R_g is given by the fit error, the latter being less than 10% of the best-fit value. For all the samples, $I(q)$ has been measured over a range of scattering wave-vectors going from $q = 5.55\ \mu m^{-1}$ to $q = 30\ \mu m^{-1}$.

Through DLS, we measured the autocorrelation function of the scattered intensity at a fixed value of $q = q_{DLS}$. At high dilution, this can be put in relation with the square of the self intermediate scattering function $F_s(\vec{q}, t)^2$, which for simply diffusive systems has the functional shape of a convolution of exponential decays, taking into account the effects of polydispersity. The analysis of $F_s(\vec{q}, t)^2$ has been performed by cumulant analysis, up to the second central moment of the distribution of decay rates:

$$F_s(\vec{q}_{DLS}, t)^2 \propto e^{-2q_{DLS}^2 \bar{D} t}\left(1 + \frac{\mu_2 t^2}{2!} + o(t^3)\right)^2, \quad [1]$$

where $\bar{D}$ is the average self-diffusion coefficient and μ_2 is related to the second moment of the distribution of D of the molecules in the sample. Using Stokes formula, we obtain the average hydrodynamic radius as $R_H = k_B T/(6\pi\eta_0 \bar{D})$, and the corresponding dispersion is $\sigma_{R_H} = \sqrt{\mu_2} R_H/(\bar{D} q_{DLS}^2)$, where k_B is the Boltzmann's constant, T the bath temperature, and η_0 is the zero-shear viscosity of the solvent. For microgels with $c = 1.37\%$, we measured the intensity time-correlation function at $q_{DLS} = 22\ \mu m^{-1}$, corresponding to an angle of 90 °, while for microgels with $c = 5.25\%$ we gathered data at both $q_{DLS} = 22\ \mu m^{-1}$ and $q_{DLS} = 15.7\ \mu m^{-1}$ (the latter corresponding to an angle of 60 °) in order to possibly detect and reject spurious effects of polydispersity when q_{DLS} was close to a value correspondent to the first minimum of the microgel form factor. The polydispersity indexes of the samples $PDI = \mu_2/(\bar{D}^2 q_{DLS}^4)$, calculated at $T \simeq 25$ °C, are as follows: 1) 0.065 for $c = 1.37$ mol% and $I_{KPS} = 1.6$ mol%, 2) 0.148 for $c = 5.25$ mol% and $I_{KPS} = 8.0$ mol%, 3) 0.074 for $c = 5.25$ mol% and $I_{KPS} = 1.6$ mol%, and 4) 0.005 for $c = 5.25$ mol% and $I_{APS} = 1.6$ mol%.

Numerical Simulations. We simulate monomer-resolved microgels of $N \sim 42{,}000$ beads exploiting a recently developed protocol (30) able to generate fully bonded, disordered polymer networks. By appropriately tuning the internal polymer distribution, the model faithfully reproduces measured swelling properties and form factors of neutral microgels across the VPT (13). The resulting network structure is made of equal-size beads, representing polymer segments interacting with the well-established Kremer–Grest potential (58). In this model, all beads experience a steric repulsion, modeled with the Weeks–Chandler–Anderson (WCA) potential:

$$V_{WCA}(r) = \begin{cases} 4\varepsilon\left[\left(\frac{\sigma}{r}\right)^{12} - \left(\frac{\sigma}{r}\right)^{6}\right] + \varepsilon & \text{if} \quad r \leq 2^{1/6}\sigma \\ 0 & \text{if} \quad r > 2^{1/6}\sigma, \end{cases} \quad [2]$$

where ε and σ are the energy and length units, respectively. Connected beads also interact via the finitely extensible nonlinear elastic potential (FENE):

$$V_{FENE}(r) = -\varepsilon k_F {R_0}^2 \log\left[1 - \left(\frac{r}{R_0\sigma}\right)^2\right], \quad r < R_0\sigma, \quad [3]$$

where $R_0\sigma = 1.5\sigma$ is the maximum bond distance and $k_F = 15$ is a stiffness parameter influencing the rigidity of the bond. These bonds cannot break during the simulation, mimicking strong covalent bonding. Beads that are linked via FENE to two neighbors represent NIPAM monomers, while those mimicking cross-linkers have fourfold valence. We analyze in detail values of the cross-linker fraction similar to the experimental ones, i.e., c = 1.25% and 5.0%. In order to be more quantitative on the c dependence of results, we also provide specific additional results for c = 3.0%, 7.5%, and 10%.

We consider that microgels obtained via free-radical polymerization embed a certain amount of ionic groups in their backbone, in this case SO_4^-, resulting from the dissociation of APS/KPS after a further thermal splitting of the ions $S_2O_8^{2-}$, starting the reaction and remaining attached to the network. This is modeled by providing a fraction f of the beads with a negative charge and inserting an equivalent number of counterions with positive charge to preserve overall electro-neutrality. Counterions sterically interact among each other and with microgel beads through the WCA potential. Their diameter is set to $\sigma_c = 0.1\sigma$ to avoid spurious effects from excluded volume (32), while electrostatic interactions are given by the Coulomb potential $V_{coul}(r_{ij}) = \frac{q_i q_j \sigma}{e^{*2} r_{ij}}\varepsilon$, where q_i and q_j are the charges of the beads, and $e^* = \sqrt{4\pi\varepsilon_0\varepsilon_r\sigma\varepsilon}$ is the reduced unit for the charge, embedding the vacuum and relative dielectric constants, ε_0 and ε_r. q_i and q_j are set to the values $-e^*$ or $+e^*$ whether it refers to charged beads or counterions. For different values of c, we consider several values for the fraction of charged monomers. We analyze in detail the case $f = 3.2\%$, corresponding to an initiator concentration $I_{KPS} = 1.6\%$mol, that matches the nominal charge content in some of the performed experiments. We also consider $f = 10\%$, a relatively high charge fraction that should mimic the experimental situation with a nominal initiator content of $I_{KPS} = 8.0\%$mol, assuming that in a synthesis process with a large quantity of highly reactive initiator radicals, a nonnegligible amount of charged groups would end up in low molecular mass by-products, which will be removed by filtration at the end of the process. For comparison, we also study the neutral case ($f = 0$) to highlight effects entirely attributable to charges. Simulations are performed for both random and surface charge distributions. In the former case, charged beads are randomly distributed throughout the network (except on cross-linkers), while for the latter they are found only on surface chains. To this aim, we randomly choose f beads located in the exterior corona, whose distance from the microgel center of mass is greater than R_g. In all simulations, the solvent is implicitly taken into account through an effective potential, which mimics the change in the polymer–solvent affinity by raising temperature:

$$V_\alpha(r) = \begin{cases} -\varepsilon\alpha & \text{if } r \le 2^{1/6}\sigma \\ \frac{1}{2}\alpha\varepsilon\left\{\cos\left[\gamma\left(\frac{r}{\sigma}\right)^2+\beta\right]-1\right\} & \text{if } 2^{1/6}\sigma < r \le R_0\sigma \\ 0 & \text{if } r > R_0\sigma, \end{cases} \quad [4]$$

where α is the solvophobicity parameter representing the effective temperature, which is varied from $\alpha = 0$ (good solvent conditions) to $\alpha \gtrsim 1.40$ (bad solvent conditions) to reproduce the swelling curve from the swollen state to the most collapsed ones. Here $\gamma = \pi\left(\frac{9}{4} - 2^{1/3}\right)^{-1}$ and $\beta = 2\pi - \frac{9}{4}\gamma$ are constants defining the functional shape of the potential (59). We showed in a previous work (33) that, for a correct description of charge effects, only neutral monomers should interact with the additional V_α potential. Instead, charged monomers retain a solvophilic character at all temperatures, i.e., for the interaction among charged beads and other charged or neutral ones we always set $\alpha = 0$. The equations of motion are integrated through a Nosé–Hoover thermostat in the constant NVT ensemble for the equilibration, and through a velocity Verlet algorithm in the constant-energy ensemble for the production runs, with an integration time-step $\Delta t = 0.002\tau$, where $\tau = \sqrt{m\sigma^2/\varepsilon}$ is the reduced time unit. All simulations are performed with the LAMMPS package (60) at fixed temperature $k_BT/\varepsilon = 1.0$. Long-range Coulomb interactions are computed with the particle–particle–particle–mesh method (61). The equilibration of each system is carried out for $2{,}000\tau$, followed by a production run of $6{,}000\tau$ from which we extracted the equilibrium averages of the main observables of interest, such as the gyration radius R_g and the density profile, defined as the average density at a fixed distance from the center of mass, $\rho(r) = \left\langle \frac{\sum_{i=1}^{N_s} \delta(|\vec{r}_i - \vec{r}_{\rm cm}| - r)}{N_s} \right\rangle$.

To estimate R_H in simulations, we instantaneously approximate the microgel as an effective ellipsoid (55) and then calculate the hydrodynamic friction using the approach developed by Hubbard and Douglas (62). For each configuration, we first compute the convex hull containing all the beads of the microgel, then evaluate the gyration tensor of all the simplices it is made of, and finally determine the ellipsoid with the same gyration tensor (55). The hydrodynamic friction ζ of each ellipsoid is calculated as follows (62):

$$\zeta = 6\pi\eta C_\Omega \equiv 6\pi\eta R_H, \quad [5]$$

where η is the solvent viscosity and C_Ω is the electrostatic capacitance. Eq. **5** is based on a solution of the Navier–Stokes equation for steady flow of rigid particles with stick boundary conditions, where the hydrodynamic interactions are described by the isotropic angular averaged Oseen tensor (62). In this approximation, the Navier–Stokes equation for the momentum flux density took the same form of the Poisson's equation for electrostatics; thereby the hydrodynamic radius becomes mathematically equivalent to the electrostatic capacitance, which for rigid ellipsoids is as follows (62):

$$R_H = C_\Omega = 2\left[\int_0^\infty \frac{1}{\sqrt{(a^2+\theta)(b^2+\theta)(c^2+\theta)}}\,d\theta\right]^{-1}, \quad [6]$$

where a, b, and c are the principal semiaxes. More details on the calculation of R_H are provided in *SI Appendix*.

To evidence the differences in the local structure of the microgels, we calculated the local swelling curve as the volume of three different regions, defined on the basis of the quantity of monomers they contain. Ordering the polymer beads according to their distance from the center of mass, at each time we associate the most inner fraction of monomers $f_{\rm m,I} = 0.65$ of beads to the core (region I), the subsequent fraction $f_{\rm m,II} = 0.20$ of them to the inner corona shell (region II), and the farthest fraction of $f_{\rm m,III} = 0.15$ beads to the outer corona shell (region III). We choose the fraction $f_{\rm m,I}$ in such a way that the core region has an overall constant density profile at all c and α values. The values of $f_{\rm m,II}$ and $f_{\rm m,III}$ are chosen in such a way that the monomers density profile at the boundary separating the two corona shells takes a value close to half the average density of the core region, to separate the more cross-linked inner part of the corona from the most external region with low-density dangling chains (*SI Appendix*, Fig. S5). The volumes of the three regions, and their outer surfaces, are calculated as the convex hulls enclosing all the beads associated to them.

To quantify the distributions of charges per chain, we calculate the chain length distribution, where each chain is defined as the sequence of monomers between cross-linkers, and we count the number of charged monomers for each chain ($q_{\rm ch}$). To build the master plot in Fig. 7, we define the extent of the minimum $\Delta_{\rm min}$ as the difference between the value of R_g/R_H at $\alpha = 0.5$ and at its minimum. We also define the average number of charges per chain on the microgel surface $\langle q_{\rm ch}\rangle_{\rm out}$, where $q_{\rm ch}$ is averaged only over chains whose distance from the microgel's center of mass is greater than R_g. To take into account screening effects, we consider the effective charge per surface chain $\langle q_{\rm ch}^{\rm eff}\rangle_{\rm out}$, that is obtained by considering an average screened charge based on the integration of the ion–counterion pair-distribution function up to a determined distance, as discussed in *SI Appendix* (*SI Appendix*, Fig. S12).

Data Availability. All study data are included in the article and/or supporting information.

ACKNOWLEDGMENTS. We thank E. Buratti, E. Lattuada, J. Ruiz-Franco, P. Schurtenberger, and F. Sciortino for valuable discussions. We acknowledge financial support from the European Research Council (Consolidator Grant 681597; MIMIC), from the European Union's Horizon 2020 Research and Innovation Programme (Grant 731019; European Soft Matter Infrastructure [EUSMI]), from the Italian Ministry of Education, University and Research (FARE Project R16XLE2X3L; SOFTART), and from Agence Nationale de la Recherche (Grant ANR-20-CE06-0030-01; THELECTRA). We gratefully acknowledge the computing time granted by EUSMI on the supercomputer JURECA at the Jülich Supercomputing Centre.

1. A. Fernandez-Nieves, H. Wyss, J. Mattsson, D. A. Weitz, *Microgel Suspensions: Fundamentals and Applications* (Wiley, 2011).
2. J. Lee *et al*., Stimuli-responsive, shape-transforming nanostructured particles. *Adv. Mater.* **29**, 1700608 (2017).
3. A. M. Mihut, B. Stenqvist, M. Lund, P. Schurtenberger, J. J. Crassous, Assembling oppositely charged lock and key responsive colloids: A mesoscale analog of adaptive chemistry. *Sci. Adv.* **3**, e1700321 (2017).
4. S. F. Medeiros, A. M. Santos, H. Fessi, A. Elaissari, Stimuli-responsive magnetic particles for biomedical applications. *Int. J. Pharm.* **403**, 139–161 (2011).
5. J. F. Quinn, M. R. Whittaker, T. P. Davis, Glutathione responsive polymers and their application in drug delivery systems. *Polym. Chem.* **8**, 97–126 (2017).
6. A. M. Wagner, D. S. Spencer, N. A. Peppas, Advanced architectures in the design of responsive polymers for cancer nanomedicine. *J. Appl. Polym. Sci.* **135**, 46154 (2018).
7. M. Wang *et al*., Assembling responsive microgels at responsive lipid membranes. *Proc. Natl. Acad. Sci. U.S.A.* **116**, 5442–5450 (2019).
8. S. Jia, Z. Tang, Y. Guan, Y. Zhang, Order–disorder transition in doped microgel colloidal crystals and its application for optical sensing. *ACS Appl. Mater. Interfaces* **10**, 14254–14258 (2018).
9. D. S. Shin *et al*., Synthesis of microgel sensors for spatial and temporal monitoring of protease activity. *ACS Biomater. Sci. Eng.* **4**, 378–387 (2018).
10. L. A. Lyon, A. Fernandez-Nieves, The polymer/colloid duality of microgel suspensions. *Annu. Rev. Phys. Chem.* **63**, 25–43 (2012).
11. R. Pelton, T. Hoare, Microgels and their synthesis: An introduction. *Microgel Suspensions: Fundam. Appl.* **1**, 1–32 (2011).
12. M. Stieger, W. Richtering, J. S. Pedersen, P. Lindner, Small-angle neutron scattering study of structural changes in temperature sensitive microgel colloids. *J. Chem. Phys.* **120**, 6197–6206 (2004).
13. A. Ninarello *et al*., Modeling microgels with a controlled structure across the volume phase transition. *Macromolecules* **52**, 7584–7592 (2019).
14. S. Seiffert, D. A. Weitz, Microfluidic fabrication of smart microgels from macromolecular precursors. *Polymer* **51**, 5883–5889 (2010).
15. G. M. Conley, P. Aebischer, S. Nöjd, P. Schurtenberger, F. Scheffold, Jamming and overpacking fuzzy microgels: Deformation, interpenetration, and compression. *Sci. Adv.* **3**, e1700969 (2017).
16. G. M. Conley, C. Zhang, P. Aebischer, J. L. Harden, F. Scheffold, Relationship between rheology and structure of interpenetrating, deforming and compressing microgels. *Nat. Commun.* **10**, 2436 (2019).
17. F. Scheffold, Pathways and challenges towards a complete characterization of microgels. *Nat. Commun.* **11**, 4315 (2020).
18. S. Bergmann, O. Wrede, T. Huser, T. Hellweg, Super-resolution optical microscopy resolves network morphology of smart colloidal microgels. *Phys. Chem. Chem. Phys.* **20**, 5074–5083 (2018).
19. M. J. Bergman *et al*., A new look at effective interactions between microgel particles. *Nat. Commun.* **9**, 5039 (2018).
20. F. Camerin *et al*., Microgels at interfaces behave as 2D elastic particles featuring reentrant dynamics. *Phys. Rev. X* **10**, 031012 (2020).
21. M. Rey, M. A. Fernandez-Rodriguez, M. Karg, L. Isa, N. Vogel, Poly-*N*-isopropylacrylamide nanogels and microgels at fluid interfaces. *Acc. Chem. Res.* **53**, 414–424 (2020).
22. M. A. Fernandez-Rodriguez, A. Martín-Molina, J. Maldonado-Valderrama, Microgels at interfaces, from mickering emulsions to flat interfaces and back. *Adv. Colloid Interface Sci.* **288**, 102350 (2021).
23. P. J. Yunker *et al*., Physics in ordered and disordered colloidal matter composed of poly(*N*-isopropylacrylamide) microgel particles. *Rep. Prog. Phys.* **77**, 056601 (2014).
24. J. Brijitta, P. Schurtenberger, Responsive hydrogel colloids: Structure, interactions, phase behaviour, and equilibrium and non-equilibrium transitions of microgel dispersions. *Curr. Opin. Colloid Interface Sci.* **40**, 87–103 (2019).

25. M. Karg *et al*., Nanogels and microgels: From model colloids to applications, recent developments, and future trends. *Langmuir* **35**, 6231–6255 (2019).
26. A. Martín-Molina, M. Quesada-Pérez, A review of coarse-grained simulations of nanogel and microgel particles. *J. Mol. Liq.* **280**, 374–381 (2019).
27. L. Rovigatti, N. Gnan, L. Tavagnacco, A. J. Moreno, E. Zaccarelli, Numerical modelling of non-ionic microgels: An overview. *Soft Matter* **15**, 1108–1119 (2019).
28. J. Oberdisse, T. Hellweg, Recent advances in stimuli-responsive core-shell microgel particles: Synthesis, characterisation, and applications. *Coll. Pol. Sci.* **298**, 921–935 (2020).
29. A. Scotti *et al*., The role of ions in the self-healing behavior of soft particle suspensions. *Proc. Natl. Acad. Sci. U.S.A.* **113**, 5576–5581 (2016).
30. N. Gnan, L. Rovigatti, M. Bergman, E. Zaccarelli, In silico synthesis of microgel particles. *Macromolecules* **50**, 8777–8786 (2017).
31. F. Camerin *et al*., Microgels adsorbed at liquid–liquid interfaces: A joint numerical and experimental study. *ACS Nano* **13**, 4548–4559 (2019).
32. G. Del Monte *et al*., Numerical insights on ionic microgels: Structure and swelling behaviour. *Soft Matter* **15**, 8113–8128 (2019).
33. G. Del Monte *et al*., Charge affinity and solvent effects in numerical simulations of ionic microgels. *J. Phys. Condens. Matter* **33**, 084001 (2021).
34. K. Haydukivska, V. Blavatska, J. Paturej, Universal size ratios of Gaussian polymers with complex architecture: Radius of gyration vs hydrodynamic radius. *Sci. Rep.* **10**, 14127 (2020).
35. C. M. Kok, A. Ruin, Relationship between the hydrodynamic radius and the radius of gyration of a polymer in solution. *Makromol. Chem.* **2**, 655–659 (1981).
36. J. Roovers, J. Martin, The hard-sphere model for linear and regular star polybutadienes. *J. Polym. Sci., B, Polym. Phys.* **27**, 2513–2524 (1989).
37. H. Senff, W. Richtering, Temperature sensitive microgel suspensions: Colloidal phase behavior and rheology of soft spheres. *J. Chem. Phys.* **111**, 1705–1711 (1999).
38. S. Nöjd *et al*., Deswelling behaviour of ionic microgel particles from low to ultra-high densities. *Soft Matter* **14**, 4150–4159 (2018).
39. D. Capriles-González, B. Sierra-Martín, A. Fernández-Nieves, A. Fernández-Barbero, Coupled deswelling of multiresponse microgels. *J. Phys. Chem. B* **112**, 12195–12200 (2008).
40. J. Zhou *et al*., Correlation between dielectric/electric properties and cross-linking/charge density distributions of thermally sensitive spherical pnipam microgels. *Macromolecules* **45**, 6158–6167 (2012).
41. O. L. Virtanen, A. Mourran, P. T. Pinard, W. Richtering, Persulfate initiated ultra-low cross-linked poly(*N*-isopropylacrylamide) microgels possess an unusual inverted cross-linking structure. *Soft Matter* **12**, 3919–3928 (2016).
42. L. Arleth, X. Xia, R. P. Hjelm, J. Wu, Z. Hu, Volume transition and internal structures of small poly(*N*-isopropylacrylamide) microgels. *J. Polym. Sci., B, Polym. Phys.* **43**, 849–860 (2005).
43. Y. Sun, Investigation of volume phase transition from the different properties of particles. arXiv [Preprint] (2005). https://arxiv.org/abs/physics/0511160 (Accessed 25 August 2021).
44. D. Truzzolillo *et al*., Overcharging and reentrant condensation of thermoresponsive ionic microgels. *Soft Matter* **14**, 4110–4125 (2018).
45. C. Huang, H. Kobayashi, M. Moritaka, M. Okubo, Hollow particles are produced by the burying of sulfate end-groups inside particles prepared by emulsion polymerization of styrene with potassium persulfate as initiator in the absence/presence of a nonionic emulsifier. *Polym. Chem.* **8**, 6972–6980 (2017).
46. E. Daly, B. R. Saunders, Temperature-dependent electrophoretic mobility and hydrodynamic radius measurements of poly(*N*-isopropylacrylamide) microgel particles: Structural insights. *Phys. Chem. Chem. Phys.* **2**, 3187–3193 (2000).
47. S. Sennato, E. Chauveau, S. Casciardi, F. Bordi, D. Truzzolillo, The double-faced electrostatic behavior of PNIPAm microgels. *Polymers* **13**, 1153 (2021).
48. M. Braibanti, C. Haro-Pérez, M. Quesada-Pérez, L. F. Rojas-Ochoa, V. Trappe, Impact of volume transition on the net charge of poly-*N*-isopropyl acrylamide microgels. *Phys. Rev. E* **94**, 032601 (2016).
49. P. van der Scheer, T. van de Laar, J. van der Gucht, D. Vlassopoulos, J. Sprakel, Fragility and strength in nanoparticle glasses. *ACS Nano* **11**, 6755–6763 (2017).
50. C. Hofzumahaus, P. Hebbeker, S. Schneider, Monte Carlo simulations of weak polyelectrolyte microgels: pH-dependence of conformation and ionization. *Soft Matter* **14**, 4087–4100 (2018).
51. A. M. Howe *et al*., Anomalous viscosity jump during the volume phase transition of poly(*N*-isopropylacrylamide) particles. *Adv. Colloid Interface Sci.* **147-148**, 124–131 (2009).
52. M. J. Bergman, J. S. Pedersen, P. Schurtenberger, N. Boon, Controlling the morphology of microgels by ionic stimuli. *Soft Matter* **16**, 2786–2794 (2020).
53. P. S. Mohanty *et al*., Interpenetration of polymeric microgels at ultrahigh densities. *Sci. Rep.* **7**, 1487 (2017).
54. A. Scotti *et al*., Hollow microgels squeezed in overcrowded environments. *J. Chem. Phys.* **148**, 174903 (2018).
55. L. Rovigatti, N. Gnan, A. Ninarello, E. Zaccarelli, Connecting elasticity and effective interactions of neutral microgels: The validity of the hertzian model. *Macromolecules* **52**, 4895–4906 (2019).
56. G. Chaudhary *et al*., Linear and nonlinear viscoelasticity of concentrated thermoresponsive microgel suspensions. *J. Colloid Interface Sci.* **601**, 886–898 (2021).
57. D. Truzzolillo, V. Roger, C. Dupas, S. Mora, L. Cipelletti, Bulk and interfacial stresses in suspensions of soft and hard colloids. *J. Phys. Condens. Matter* **27**, 194103 (2015).
58. G. S. Grest, K. Kremer, Molecular dynamics simulation for polymers in the presence of a heat bath. *Phys. Rev. A Gen. Phys.* **33**, 3628–3631 (1986).
59. T. Soddemann, B. Dünweg, K. Kremer, A generic computer model for amphiphilic systems. *Eur. Phys. J. E* **6**, 409–419 (2001).
60. S. Plimpton, Fast parallel algorithms for short-range molecular dynamics. *J. Comput. Phys.* **117**, 1–19 (1995).
61. M. Deserno, C. Holm, How to mesh up Ewald sums. I. A theoretical and numerical comparison of various particle mesh routines. *J. Chem. Phys.* **109**, 7678–7693 (1998).
62. J. B. Hubbard, J. F. Douglas, Hydrodynamic friction of arbitrarily shaped Brownian particles. *Phys. Rev. E* **47**, R2983 (1993).